Global Modeling of Spur Formation in Spiral Galaxies

Rahul Shetty and Eve C. Ostriker

Department of Astronomy, University of Maryland, College Park, MD 20742-2421

shetty@astro.umd.edu, ostriker@astro.umd.edu

ABSTRACT

We investigate the formation of substructure in spiral galaxies using global MHD simulations, including gas self-gravity. Local modeling by Kim and Ostriker (2002) previously showed that self-gravity and magnetic fields cause rapid growth of overdensities in spiral arms; differential compression of gas flowing through the arms then results in formation of sheared structures in the interarms. These sheared structures resemble features described as spurs or feathers in optical and IR observations of many spiral galaxies. Global modeling extends previous local models by including the full effects of curvilinear coordinates, a realistic log-spiral perturbation, self-gravitational contribution from 5 radial wavelengths of the spiral shock, and variation of density and epicyclic frequency with radius. We show that with realistic Toomre Q values, self-gravity and galactic differential rotation produce filamentary gaseous structures with kpc-scale separations, regardless of the strength – or even presence – of a stellar spiral potential. However, a sufficiently strong spiral potential is required to produce "true spurs", consisting of interarm structures emerging from gas concentrations in the main spiral arms. In models where Q is initially constant, filaments due to interarm self-gravity grow mainly in the outer regions, whereas true arm spurs grow only in the inner regions. For models with $Q \propto R$, outer regions are intrinsically more stable so "background" interarm filaments do not grow, but arm spurs can develop if the spiral potential is strong. Unlike independently-growing "background" filaments, the orientation of arm spurs depends on galactic location. Inside corotation, spurs emanate outward, on the convex side of the arm; outside corotation, spurs grow inward, on the concave side of the arm. Based on orientation and the relation to arm clumps, it is possible to distinguish "true spurs" that originate as instabilities in the arms from independently growing "background" filaments. We measure spur spacings of $\sim$3 - 5 times the Jeans length in the arm,

and arm clump masses of $\approx 10^7 M_\odot$. Finally, we have also studied models without self-gravity, finding that magnetic fields suppress a purely hydrodynamic instability recently proposed by Wada & Koda (2004) as a means of growing interarm spurs and feathers. Our models also suggest that magnetic fields are important in preserving grand design spiral structure when gas in the arms fragments via self-gravity into GMCs.

Subject headings: galaxies: ISM – galaxies: structure – ISM: kinematics and dynamics – instabilities – MHD

1. Introduction

Observations of disk galaxies reveal that arm substructures are prevalent in grand design spirals. Some of the most prominent secondary features are spurs and feathers, which are structures that emanate from the primary spiral arm and are usually seen to sweep back to trail the flow in the interarm region. Historically, in the observational literature the term "spur" has denoted stellar features seen in optical emission (Elmegreen 1980), whereas the term "feathering" has been used to denote a series of extinction features that overlies the bright portion of a stellar spiral arm (Lynds 1970). Elmegreen (1980) concluded that spurs are long-lived features, based on observations in multiple bands, including the I band, which generally traces the older stellar component. Recent high-resolution observations, such as the Hubble Heritage image of M51 (Scoville & Rector 2001) and several galaxies in the Spitzer SINGS sample (Kennicutt et al. 2003), have revealed examples of these features in extraordinary detail. An archival study of HST images has established that spurs and feathers are in fact ubiquitous in galaxies with well-defined spiral arms and that single continuous structures evidence evolution from primarily gaseous to primarily stellar composition (La Vigne et al. 2006). Taken together, these observations indicate that feathers and spurs are an essential aspect of spiral structure that should be accounted for by theoretical modeling of disk galaxies.

Many studies of spiral structure, both theoretical and observational, have applied the hypothesis of a Quasi Stationary Spiral Structure (QSSS) (Lin & Shu 1964). Under the QSSS framework, the general shape of the spiral pattern is assumed to remain steady for many galactic revolutions. The stellar spiral arms themselves arise as self-consistent density waves (or modes). Roberts (1969) demonstrated that shocks can develop in the gaseous component as it responds to an "external" spiral potential arising from the stellar disk, and predicted values of the gas velocity both upstream and downstream from the shocks. Such velocity profiles have been observed for many galaxies, such as M51 (e.g. Rand 1993, Aalto

et al. 1999, Shetty et al. 2006), and M100 (e.g. Rand 1995). M81 has also been studied extensively in support of density wave theory (e.g. Visser 1980 and Lowe et al. 1994).

A number of theories consistent with the QSSS concept have been proposed to explain substructure in spiral galaxies. Shu, Milione, & Roberts (1973) suggest that ultra-harmonic resonances between the motion of the primary spiral pattern and the background gas flow can be responsible for the secondary features in spiral galaxies. Chakrabarti, Laughlin, & Shu (2003, hereafter CLS) performed hydrodynamic simulations of self-gravitating gaseous disks to study the role of ultraharmonic resonances. They showed that the spiral arm bifurcates and strong branches, which in observations are large scale dust lanes that are similar in angular extent to the main arms, occur near resonant radii (see also Artymowicz & Lubow 1992).

The origin and nature of observed smaller-scale feathers and spurs, however, has not yet been firmly established. Balbus (1988) attributed these features to growth of gravitational instabilities in the gas component in preferred directions. Kim & Ostriker (2002), hereafter KO, performed numerical simulations focused on a local patch of a gaseous spiral arm in a galactic disk, and showed that the growth of prominent, nonlinear spurs[1] can occur due to the mutual contributions of self-gravity and magnetic fields, via the so-called "Magneto-Jeans Instability." Within the arm, the radial gradient in angular velocity is reversed, so that spurs in the models of KO are initially locally leading. Well into the interarm regions, background galactic shear causes the spurs to become trailing features. This characteristic shape is evident in the Hubble Heritage image of M51 (Scoville & Rector 2001). On the other hand, Wada & Koda (2004), hereafter WK, suggest that the growth of spurs results from purely hydrodynamic effects. In their two-dimensional models (excluding magnetic fields and self-gravity), the spiral shocks become unstable; this instability causes the growth of clumps and subsequently leading interarm features, which they refer to as spurs. They suggest the mechanism responsible for the growth of these spurs is the Kelvin-Helmholtz instability. Using SPH simulations, Dobbs & Bonnell (2006) also investigate the non-self-gravitating case, and suggest that feather and spur formation requires gas temperatures < 1000K. Contemporary with the current work, Kim & Ostriker (2006) extended their 2D local self-gravitating models to 3D; that work also investigates the effects of vertical structure on hydrodynamic Kelvin-Helmholtz modes.

Here, we model isothermal gaseous disks under the influence of both magnetic and self-gravitational effects. We extend the local simulations of KO into the global regime, which

---

[1]We adopt the term "spur", following KO, to describe interarm gas features in hydrodynamic and MHD models.

allows us to study the growth of spurs using more realistic models. In particular, whereas in KO the unperturbed disk had uniform density, a linear shear profile, and did not treat curvature effects, the present models relax all of these idealizations. Our global models, which extend over more than an order of magnitude in radius, allow arbitrary density profiles and rotation curves, and solve the full equations of magnetohydrodynamics (MHD) in cylindrical symmetry. To assess the effect of self-gravity, we first consider just a disk of rotating gas, varying initial conditions such as the magnetic field strength and Toomre stability parameter. We then apply an external spiral potential, which reorganizes the gas to form a spiral pattern. In models with and without a spiral potential, we follow the evolution of the gas far into the nonlinear domain as self-gravity takes hold, investigating the properties of the interarm features and clumps that arise.

This paper is organized as follows: In §2 we present the relevant equations of MHD and gravity, and describe the models, parameters, and numerical algorithms we use to simulate disk galaxies with spiral arms. In the following section (§3), we consider models without including self-gravity, both with and without magnetic fields. Next, in §4, we present the models including self-gravity. We show how self-gravity causes the growth of condensations in the gas, and how this effect is crucial for the growth of interarm structures in disks with an external spiral potential. In §5 we analyze and discuss various aspects of our results, including: in §5.1, we explore the issue of distinguishing whether observed interarm structures are true arm spurs or independent background features with a superposed large-scale spiral structure; in §5.2 we quantify masses and spacings of clumps and spurs; and in §5.3 and §5.4 we discuss the issue of gas/star arm offsets and disk thickness, respectively. We conclude in §6 with a summary. Finally, in the Appendix, we give a detailed description of our algorithms to compute self-gravity, as well as tests comparing the results of different numerical approaches.

2. Modeling Methods

2.1. Basic Equations

Our simulations involve the gaseous response to an external spiral potential, including effects of self-gravity and magnetic fields, in a two-dimensional galactic disk model. The gas is initially in pure circular motion around the galactic center. We adopt a flat rotation curve, i.e. a constant azimuthal velocity v_c. A non-axisymmetric variation in the stellar component is responsible for an external spiral perturbation, and is modeled as a rigidly rotating potential with a pattern speed Ω_p. We investigate the formation and evolution of arms, spurs, clumps, and other features by integrating the MHD equations in a polar (R, ϕ) coordinate system.

The relevant equations of MHD and gas self-gravity are

$$\frac{\partial \Sigma}{\partial t} + \nabla \cdot (\Sigma \mathbf{v}) = 0, \tag{1}$$

$$\frac{\partial \mathbf{v}}{\partial t} + \mathbf{v} \cdot \nabla \mathbf{v} + \frac{1}{\Sigma} \nabla p = \frac{2H}{4\pi\Sigma}(\nabla \times \mathbf{B}) \times \mathbf{B} - \nabla(\Phi_{ext} + \Phi), \tag{2}$$

$$\frac{\partial \mathbf{B}}{\partial t} = \nabla \times (\mathbf{v} \times \mathbf{B}), \tag{3}$$

$$\nabla^2 \Phi = 4\pi G \delta(z)\Sigma. \tag{4}$$

Here, Σ is the gas surface density, and $\mathbf{v}$, p, and $\mathbf{B}$ are the vertically averaged velocity, vertically integrated pressure, and vertically averaged magnetic field, respectively. The semi-thickness of the disk is H, such that $\Sigma/2H$ is the mid-plane density ρ_0. For our models, we assume an isothermal equation of state, so that $p = c_s^2 \Sigma$, where c_s is the sound speed. The terms Φ_{ext} and Φ, respectively, represent the external spiral potential and the gaseous self-gravitational potential. The external spiral potential Φ_{ext} is specified at time t, in the inertial frame, by

$$\Phi_{ext}(R, \phi; t) = \Phi_{ext,0} \cos[m\phi - \phi_0(R) - m\Omega_p t] \tag{5}$$

where m, $\phi_0(R)$, and Ω_p are the number of arms, reference phase angle, and spiral pattern speed, respectively. We assume the spiral arms have a constant pitch angle i, implying a logarithmic spiral, so that

$$\phi_0(R) = -\frac{m}{\tan i} \ln(R) + constant. \tag{6}$$

Since we simulate disks in an inertial frame of reference, explicit corrections to equation (2) for Coriolis and centrifugal forces are not required.

2.2. Model Parameters

For the simulations presented in this paper, we use a constant sound speed c_s, which we set to 7 km s^{-1} for scaling our solutions. We use a constant rotational velocity v_c, which is set to 210 km s^{-1}. Because our models are isothermal, in fact our results would hold for any model with the same ratio $v_c/c_s = 30$. The code length unit is L_0, which for convenient scaling of our solutions we set to 1 kpc. With $c_s = 7$ km s^{-1}, this implies a time unit for scaling of $t_0 = L_0/c_s = 1.4 \times 10^8$ years. This time corresponds to one orbit $t_{orb} = 2\pi/\Omega_0$ at a fiducial radius R_0 which is given by $R_0 = L_0 v_c/2\pi c_s$. With $L_0 = 1$ kpc, the value of R_0 is 4.77 kpc. Our results can be rescaled to other values of R_0 and L_0 with the same ratio.

We explore a range of values for the parameters required to specify the spiral perturbation. The amplitude of the potential perturbation $\Phi_{ext,0}$ in equation (5) is characterized by the ratio F of the maximum radial perturbation force to the radial force from the background axisymmetric potential (responsible for v_c), i.e.

$$F \equiv \frac{\Phi_{ext,0}m}{v_c^2 \tan i}. \tag{7}$$

We model spiral disks with external potential strengths $F = 10\%$, 3%, and 1%. We apply the spiral perturbation gradually, increasing from zero and settling to the maximum level F at time $t = t_{orb}$. Since it has proved to be difficult to locate corotation from observations, we also explore a range in $\Omega_p/\Omega_0 = 0.19$ to 0.96. For our fiducial values of L_0 and c_s, Ω_p ranges from ~ 8 to 42 km s^{-1} kpc^{-1}, corresponding to corotation radii of 25 to 5 kpc for a circular velocity of 210 km s^{-1}. The pitch angle i in most of our simulations is $10°$. We will show that changing the pitch angle does not strongly affect the formation and properties of substructures. For all our models, we have an $m = 2$ (two-armed) pattern.

The initial surface density Σ_0 at the fiducial radius R_0, along with the constant circular velocity v_c, determines the value of the Toomre stability parameter at R_0,

$$Q_0 \equiv \frac{\kappa_0 c_s}{\pi G \Sigma_0}, \tag{8}$$

where κ_0 is the initial epicyclic frequency; for a constant circular velocity, $\kappa_0 = \sqrt{2}\Omega_0 = \sqrt{2}v_c/R_0$. Thus, the initial background surface density at R_0 is

$$\Sigma_0 = \frac{32}{Q_0} M_\odot \, \mathrm{pc}^{-2} \left(\frac{c_s}{7 \, \mathrm{km\,s^{-1}}}\right) \left(\frac{\kappa_0}{62 \, \mathrm{km\,s^{-1}\,kpc^{-1}}}\right). \tag{9}$$

As described below, we explore a couple of initial density distributions, including a $\Sigma \propto R^{-1}$ density distribution for which Q is initially constant for the whole disk.

We characterize the initial magnetic field strength by the ratio β of the midplane gas pressure to the midplane magnetic field pressure

$$\beta = \frac{P_{gas}}{P_B} = \frac{8\pi c_s^2 \Sigma}{2HB^2}. \tag{10}$$

The initial magnetic field lines $\mathbf{B} = B\hat{\phi}$ lie in the plane of the disk, and are directed in the $\hat{\phi}$ direction only. From equation (10) the value of the magnetic field (with c_s, β, and H constant) varies $\propto \Sigma^{1/2}$. Taking $H = 100$ pc and $Q_0 = 2$, the value of B at the fiducial radius is

$$B_0 = \left(\frac{4c_s^3 \kappa_0}{Q_0 H G \beta}\right)^{1/2} = \frac{8.2}{\sqrt{\beta}} \, \mu G. \tag{11}$$

2.3.   Numerical Methods

We follow the evolution of the gaseous disk by integrating equations (1) - (4) using a cylindrical polar version of the ZEUS code. ZEUS (Stone & Norman, 1992a, 1992b) is a time-explicit, operator-split, finite difference method for solving the equations of MHD on a staggered mesh. ZEUS employs "constrained transport" to ensure that $\nabla \cdot \mathbf{B} = 0$, and the "method of characteristics" for accurate propagation of Alfvénic disturbances. The hydrodynamic/MHD portion of our cylindrical-polar code has been verified using a standard suite of test problems. These include advection tests, shocks aligned and not aligned with the coordinates, a magnetized rotating wind (Stone & Norman 1992b), and a rotating equilibrium disk with both magnetic and pressure gradients.

The (R, ϕ) staggered mesh for our version of the code has a constant logarithmic increment in the radial dimension, i.e. $R_{i+1} = (1 + \delta)R_i$, for some $\delta > 0$. We consider only the perturbed gas density (by subtracting off the initial density) in determining the self-gravitational potential at each timestep. The contribution of the initial axisymmetric gas disk to the total potential is assumed to be included in the axisymmetric potential responsible for the constant circular velocity v_c. To compute the self-gravitational potential Φ, we use one of two methods described in the Appendix. One method uses a combination of a Fourier transform in the azimuthal direction and a Green's function in the radial direction, while the other method uses Fourier transforms in both directions on an expanded, zero-padded grid. For both methods, we allow for finite disk thickness using a softening parameter H. Except as noted, we adopt $H = 100$ pc. We give detailed descriptions of our methods, tests, and comparisons in the Appendix. Fast Fourier transforms are performed using the free software FFTW (Frigo & Johnson 2005).

The standard computational domain for our models has 512 radial and 1024 azimuthal zones, covering a radius range of 1 - 15 kpc, and an azimuthal range of 0 - π radians. With this resolution, the Jeans length ($\lambda_J = c_s^2/G\Sigma$) from our initial surface density distributions are well resolved at all radii, satisfying the Truelove criterion (Truelove et al. 1997). The radial range allows ≈ 5 radial wavelengths of the spiral pattern. Given the extended range in the radial dimension, we implement outflow boundary conditions, since loss of gas at the boundary will not affect the majority of the disk. We also taper the spiral potential near the boundaries, which helps minimize loss of matter near the edges. In the azimuthal direction, we use periodic boundary conditions. Though the azimuthal range is only half of a complete disk, the gravitational potential includes the contribution from the other half that is not explicitly simulated (see Appendix).

3. Simulating Spiral Galaxies Without Gas Self-Gravity

We first investigate the flow of gas in a spiral potential without including the gaseous self-gravitational potential. These preliminary simulations will indicate whether, for a given parameter set and numerical resolution, long lasting spiral patterns can be sustained. We will also investigate the effect of magnetic fields on the resulting flow and spiral morphology. As these models are similar to the hydrodynamic simulations of WK, we are able to investigate the "wiggle instability" that they propose, and to assess how magnetic fields affect this process. Table 1 shows the relevant parameters used for each model. Column (1) labels each model. Column (2) lists β, which characterizes the magnetic field strength (see eq. [10]). The external potential strength F (from eq. [7]) is listed in column (3). Column (4) gives the pattern speed Ω_p (used in eq. [5]). The pitch angle i is listed in column (5). We note that though the computational domain only simulates half the disk, with periodic azimuthal boundary conditions, we replicate the simulated half in presenting snapshots of the models.

3.1. Pure Hydrodynamic Models

We begin by considering simple cases where the rotating gas in a disk only responds to an external spiral potential, without including magnetic fields or gas self-gravity. Model HD1 has a weak ($F = 3\%$) and slowly rotating external spiral potential, as well as a small pitch angle (10°). Figure 1 shows density snapshots of model HD1. At $t/t_{orb} = 1$, when the external potential reaches its maximum amplitude, the spiral arms are weak but distinct. Figures 1(b) and 1(c) shows that 2 orbits after the potential is fully applied, the spiral arms are still distinct and rather regular. At $t/t_{orb} = 3$, in the inner regions, shown in Figure 1(d), the spiral arms are not as distinct as the rest of the galaxy. The main arms grow weaker, and leading spiral like features grow between the main (trailing) arms. Nevertheless, a global spiral pattern persists throughout the galaxy, indicating that a weak perturbing potential can sustain a global, long lasting, spiral pattern.

Figure 2 shows density snapshots of model HD2, with the same scale shown in Figure 1 for model HD1. As expected, since F is increased to 10 %, the spiral arms are much stronger. The global pattern persists for many orbits, but the arms are clearly more dynamic. As early as 1 orbit after the potential is fully applied (at $t/t_{orb} = 2$), the spiral arms at $\sim$7.5 kpc, indicated by the arrow in Figure 2(b), bifurcates. This region is near the Inner Lindblad Resonance (ILR). The bifurcation causes the arm at $\sim$7 kpc to lose matter, and it thus becomes weaker than the arms located farther inward. Further, the arm at $\sim$9.3 kpc has a much different pitch angle from the arms at different locations. After an additional orbit, the bifurcated part of the inner arm has moved radially outward and connected with the

outer arms. In the meantime, the arms that lost matter during bifurcation regain strength and attain similar surface density to the arms in the inner regions.

Figure 2(d) shows the central regions of model HD2 at $t/t_{orb} = 3$. Here, unlike in the case with a weaker potential (Fig. 1(d)), the arms remain continuous and distinct. However, there are also prominent interarm filamentary features, some even connecting two adjacent arm segments. Such features can be seen to develop as early as $t/t_{orb} = 2$, in Figure 2(b). WK found similar features, which they identified as spurs/fins, in their hydrodynamic models (the detailed morphology differs because they use a different rotation curve). They attribute the formation of their spurs/fins to the Kelvin-Helmholtz instability. In our models, these features only grow in the innermost regions; we shall show in the following section that magnetic fields prevent their formation.[2] We shall further show that it is the combination of magnetic fields *and* self-gravity that results in spurs forming everywhere in a disk, not just in the innermost regions.

Another difference between models HD1 and HD2 is the relative location of the gas density peaks of the arms. The gaseous arms in model HD1 ($F = 3\%$) form farther downstream than in model HD2 ($F = 10\%$). We discuss the offset between the dust lanes and the spiral potential minimum in §6, as well as compare with the results from the recent study by Gittins and Clarke (2004).

Changing the pattern speed of the spiral potential does not dramatically alter the resulting spiral structure. Figure 3(a) shows a snapshot of model HD3, one orbit after the external spiral potential with $F = 10\%$ is fully applied. Here, the corotation radius is at 5 kpc, instead of 25 kpc. The spiral structure is similar to that shown in Figure 2(b), but the arms are not as dynamic, and the bifurcation region is shifted inward, as expected if this phenomenon is indeed due to a resonance. For all our models the shock locus transitions from the concave to the convex side of the gaseous arm at or near corotation. Inside this radius, the shock front is located on the concave side of the gaseous spiral arm. Farther out in the disk, the shock front moves to the outer, convex side of the arm.

Figure 4 shows the density and velocity profiles relative to the external spiral potential in two regions inside and outside corotation for model HD3. For both regions, the gas peaks occur downstream from the minimum of Φ_{ext}. Inside corotation, the gas shocks after the gas passes through the spiral potential. Outside corotation, the spiral pattern passes through the gas, leaving the shocked gas behind. The shock front itself is always upstream from the density peak. Thus, inside corotation the shock occurs on the inside face of the spiral

---

[2]Recent models by Kim & Ostriker (2006) have also shown that the instability identified by WK is suppressed by three-dimensional effects even in unmagnetized models.

arm, while outside corotation the shock forms on the outer face of the arm. The density and velocity profiles in Figure 4 are quite similar to those obtained using local models (e.g. Figs. 2, 3 of KO). We note that in regions closer to corotation, the gas peaks lie near the minimum in Φ_{ext}, and shocks cannot be clearly distinguished.

The secondary density hump in the profile inside corotation occurs near the 4:1 ultraharmonic resonance, where $\Omega_p - \Omega = -\kappa/4$ (if pressure effects are ignored). CLS also identified similar secondary features in their global hydrodynamic models, which they denote as "branches." They also find such branches near locations of the 6:1 ultraharmonic resonance. Qualitatively, the formation and subsequent evolution of the branch features in our models are similar to those shown in CLS.

Models with a larger pitch angle show some differences from those with more tightly wrapped arms. Figure 3(b) is a snapshot of model HD4, again 1 orbit after the full spiral potential is applied. Similar to the results of WK, this model shows that loosely wound spiral arms are much more unstable than tightly wound arms, because the shock is stronger. The bifurcation is clearly evident, and results in replenishment of the depleted arms in the outer regions after an additional orbit. The interarm sheared filamentary features in the inner region of the galaxy are more pronounced than in the corresponding model with $i=10°$, shown in Figure 2(b).

3.2.   Magnetohydrodynamic Models

Before including self-gravity, we test the effect of magnetic fields on non-self-gravitating disks with a spiral potential. Figure 5 compares snapshots at $t/t_{orb} = 2.0$, of a model without magnetic fields, HD2, to one with magnetic fields, MHD1. Clearly, the interarm features described in the previous section no longer appear in the magnetized case. Thus, equipartition-strength magnetic fields are able to suppress the "wiggle instability" identified by WK in large F simulations (for small enough F, as seen in model HD1, there is stability even in unmagnetized models).

4.   Models Including Gas Self-Gravity

To include self-gravity in our simulations, we must introduce an additional parameter, which we choose to be the Toomre parameter Q_0 evaluated at R_0, given in equation (8). Table 2 shows the input parameters for models including self-gravity. The first five columns are the same as those in Table 1, and column (6) gives the value of Q_0. As shown in equation

(8), $Q \propto \kappa/\Sigma$.

4.1. Disk Stability Tests for Constant Q Models

For disks with constant circular velocities, the epicyclic frequency $\kappa \propto R^{-1}$; thus if the initial density distribution $\Sigma \propto R^{-1}$, Q will be constant for the whole disk. We first consider models in which the initial surface density profiles are indeed inversely proportional to the galactocentric radius. Such a distribution is consistent with many surface density profiles shown in Regan et al. (2001) and Wong & Blitz (2002).

To test the inherent stability of disks with constant Q, we consider cases with self-gravity, but with no external potential, models SHDne1, SHDne2, and SMHDne, shown in Figure 6. Since the initial density has random white-noise 0.1% perturbations, the over-dense regions can grow due to self-gravity. As these regions grow, they also become stretched azimuthally due to the background shear. The runaway growth of the over-dense regions eventually causes neighboring regions to have extremely large velocities, such that the Courant condition would require an extremely small timestep; we therefore halt the simulation. Model SHDne1 has $Q_0=1$, and becomes unstable very rapidly (within one orbit at R_0), as shown in Figure 6(a). Figure 6(b) shows model SHDne2, with $Q_0 = 2$, at the same time as the $Q_0 = 1$ model in Figure 6(a). Since the $Q_0 = 2$ model is more stable, enough time has not yet elapsed for the over-dense regions to dominate.

The addition of magnetic fields, as shown in Figure 6(c) from model SMHDne with $Q_0 = 1$, does not affect the growth of filaments significantly. The subtle difference is that the magnetic fields slightly slow the growth of over-dense regions. As a result, models including magnetic fields evolve longer before the flow velocities in some zones becomes extreme. Figure 6(d) is the last snapshot of model SHDne2 at $t/t_{orb} = 1.5$ orbits. Here, the outer regions have evolved to the point that the structure is similar to that in Figure 6(a). However, it is clear that the radius of the stable inner region in the $Q_0 = 2$ model is larger than that of the $Q_0 = 1$ model (SHDne1). As expected, increasing the value of Q_0 increases the area of stability in the inner regions, and requires more time for the instability in the outer regions to grow.

The stability tests show that filament-like structures will grow in a shearing disk with sufficient gas surface density, regardless of the presence of magnetic fields. The Toomre stability parameter governs which regions are prone to gravitational instabilities. As Q_0 increases, the outer disk becomes more stable, and more time is required for growth of instabilities. In the models presented thus far, we have considered disks for which the initial

surface densities vary as R^{-1}, so that Q is initially constant everywhere in the disk. The reason that the outer disk becomes unstable even when the inner disk does not is that the disk thickness H is constant throughout the disk. The finite thickness stabilizes the inner disk more than the outer disk, because the ratios of H/λ_T and H/λ_J vary as R^{-1} for constant Q models, where the Toomre wavelength $\lambda_T = 4\pi^2 G\Sigma/\kappa^2$ and the Jeans wavelength $\lambda_J = c_s^2/G\Sigma$. We discuss this effect in §5.4.

4.2. Disk Stability Tests for $Q \propto R$ Models

The models we have presented so far have an initial surface density distribution proportional to R^{-1}, yielding a constant value of the Toomre parameter with R. However, the surface density distributions shown by Wong & Blitz (2002) are in many cases approximately consistent with a surface density distribution proportional to R^{-2}. Further, in the observational analysis of Martin & Kennicutt (2001), Q varies with radius for many galaxies. A variety of radial distributions are evident, some close to R^{-1} and others to R^{-2}. We thus consider models similar to those presented thus far, but with initial R^{-2} surface density distributions, such that $Q \propto R$. The labels of such models will follow the convention of those already presented, but with the addition of a prime (ʹ) sign.

Figure 7 shows snapshots of disk models without an external potential, SHDne1ʹ and SHDne2ʹ, at $t/t_{orb} = 1.0$. For SHDne1ʹ, the value of Q ranges from 0.21 at the inner boundary to 3.15 at the outer boundary. The respective values are twice as large in model SHDne2ʹ. When compared with Figure 6, it is clear that these models are much more stable. Only the innermost region in SHDne1ʹ shows more instability than SHDne1, the corresponding disk with Σ initially $\propto R^{-1}$ (Fig. 6(a)). As expected, since Q increases with R, the outer regions of the disk are more stable, and thus less susceptible to gravitational instabilities. In fact, there has been very little growth of perturbations in model SHDne2ʹ ($Q_0 = 2$) at 1 orbit (Fig. 7(b)). However, given enough time, the instabilities eventually begin to grow in this disk, and will appear similar to the snapshot in Figure 7(a).

4.3. Spiral Models with Constant Q

To investigate the interaction between gaseous self-gravity and the global spiral structure, we focus our presentation on six spiral models with parameters shown in Table 2. In addition to these models, we have performed additional simulations with a wide range of values and combinations of the chosen parameters, with similar characteristic results. For

our fiducial model, $\beta = 1$, $\Omega_p = 8.4$ (corresponding to a corotation radius of 25 kpc, which is outside the edge of the disk), $i = 10°$, and $Q_0 = 2$. The external potential strength F will be indicated, as will cases where the other parameters differ from the fiducial one.

Figure 8 shows the fiducial model with $F = 3\%$ and $F = 10\%$, SMHD1 and SMHD2, respectively, at $t/t_{orb} = 1.0$ and 1.125. The most striking aspect of the snapshots, besides the spiral arms, are the interarm features. These features differ significantly between the two models, with differences enhanced at the later times. This is shown for the central region in detail in Figure 9. With a weak external potential (SMHD1), the interarm features are strong as far inwards as 7 kpc. However, with the strong external potential (SMHD2), the interarm features are strong in the outer regions, but at radii of $\sim$5 - 11 kpc they are weak. In the inner regions, at $R \lesssim 5$ kpc, the interarm features are again much stronger than the background; there are no strong interarm features in the innermost region of SMHD1. The reason for this difference in interarm features is clear in the structure of the arms themselves. In the $F = 3\%$ model, the arms inside 7 kpc are smooth. In the $F = 10\%$ models, on the other hand, the arms are broken into many clumps. The strong external potential in model SMHD2 has gathered more matter into the spiral arms, and self-gravity causes concentrations to grow, with much of the gas eventually collapsing into clumps. Gas flowing through the arms can be concentrated by these growing clumps, and returned to the interarm regions as overdense spurs. Since the stronger spiral potential of model SMHD2 concentrates more gas in the arms, the interarm regions at radii of $\sim$5 - 11 kpc has less gas compared to model SMHD1 with a weak spiral potential; as a result the interarm features in this region are weaker in model SMHD2.

The boxed region from Figure 9(b) is shown in detail in Figure 10 with the instantaneous velocities, including the unperturbed velocity field. Far from the spiral arms, the instantaneous velocities do not differ much from the initial circular velocities. As expected, the velocities of gas near the arms is significantly perturbed. Further, the over-dense clumps in the arm flow along the arm. At this stage, gravitationally bound structures do not leave the gaseous spiral arm, but continue to build in mass as matter from the interarm regions flows into the arm. If kept unchecked, the arm clumps would grow in a runaway fashion.

The overlaid contours in Figure 10 indicate magnetic field lines. Initially, the magnetic field is directed only in the azimuthal direction. As the spiral arms increase in density, the magnetic field is concentrated in the arms, thereby weakening the field in the interarms. The growth of the clumps along the arms further perturbs the field lines. However, only strong density enhancements produce field perturbations; the interarm features emerging from the clumps and the background features that grow in models without an external spiral potential do not strongly affect the magnetic field.

Figure 11 shows snapshots from a model without magnetic fields. Both the interarm features and clumps within the arms grow much more rapidly compared with the corresponding model with magnetic fields, SMHD2 (in Fig. 8). As early as $t/t_{orb} = 1.0$, the arm coherence in the outer regions is weakened due to the rapid growth of over-dense regions. Even in models with $\beta = 10$ (not shown here), the arms rapidly fragment. Similar to the models without self-gravity, strong magnetic fields act to preserve the overall arm shape, and suppress the growth of interarm features, either those caused by self-gravity, or by hydrodynamic effects.

Interarm features also grow more rapidly as the initial Toomre parameter Q_0 is reduced. Figure 12 shows the snapshots of SMHD3, a model similar to model SMHD2 except that $Q_0 = 1$ instead of 2. Even though this model has magnetic fields, the interarm features still grow relatively rapidly. Similar to low Q models without an external potential, this model is more susceptible to the growth of perturbations at smaller radii than the $Q_0 = 2$ model.

We have also explored models with varying values of the pattern speed and spiral pitch angle. Figure 13(a) shows snapshots after 1 orbit of model SMHD4. Model SMHD4 is similar to the fiducial model SMHD2, except that $\Omega_p = 42$ km s^{-1} kpc^{-1}. The corotation radius for such a pattern speed is 5 kpc. Upon first glance, this snapshot may seem rather similar to the snapshot of model SMHD2 in Figure 8. However, in regions outside corotation the interarm features protrude inwards, towards the galactic center. The arms still have the over-dense knots, but the stretched features near the arms project in the opposite direction from those in the fiducial model. This is as expected, because outside corotation, the rotating spiral potential has a greater angular velocity than the gas. The flow enters the arms from the outer (convex) side, and leaves from the inner (concave) side. Azimuthally varying over/under dense regions that are created within the arm and return to the interarm region on the inside of the arm are sheared into trailing structures. This reversed orientation is even more apparent in models where the Toomre parameter $Q \propto R$, presented in §4.4. The trailing features in the outermost part of the disk arise in a different way, however, as we shall discuss in §5.

Model SMHD5, shown at $t/t_{orb} = 1$ in Figure 13(b), is similar to the fiducial model but with a larger pitch angle of $i = 20°$. Besides the expected difference in shape of the spiral arms, many of the other features evident in SMHD2 (in Figs. 8(c) and (d)), such as the knots of matter in the arm and the trailing features in the outermost and innermost regions, are also present.

4.4.   Spiral Models with $Q \propto R$

For spiral models with initial surface density distributions $\propto R^{-2}$, we only present cases with magnetic fields ($\beta = 1$); we have shown that magnetic fields act to keep the arms intact. Otherwise, self-gravity causes the runaway growth of the clumps in the arms. Figure 14 shows snapshots of model SMHD3$'$ ($Q_0 = 1$) and SMHD2$'$ ($Q_0 = 2$). Comparing with Figures 8, 9, and 12, these models are much more stable in the outer regions, as expected. Nevertheless, strong interarm trailing structures do grow in the inner $(14 \text{ kpc})^2$. Since these models are more stable, the interarm features do not extend as for away from the spiral arms as those in the constant Q models. These features grow in both $Q_0 = 1$ and $Q_0 = 2$ models, but are stronger in the $Q_0 = 2$ case. It is also clear that the interarm features connect with the most dense clumps in the arms, which are more dense in model SMHD2$'$ than SMHD3$'$.

Even though the self-gravitational force is stronger in model SMHD3$'$ ($Q_0 = 1$) than in model SMHD2$'$ (because the absolute Σ is larger in SMHD3$'$), the clumps in the arms of model SMHD2$'$ are more dense (relative to Σ_0). This results because more gas flows into the spiral arms in the more stable disk of model SMHD2$'$. As shown from the corresponding disk stability tests in Figure 7, the inner regions of models with $Q_0 = 1$ are much more unstable than models with $Q_0 = 2$. These background instabilities will grow regardless of the presence of an external spiral potential. For a stable disk as in model SMHD2$'$, stability of the background disk allows more gas to flow into the arms, resulting in stronger arms as well as clumps.

Figure 15 shows a snapshot of model SMHD4$'$, with large pattern speed ($\Omega_p = 42$ km s^{-1} kpc^{-1}) at $t/t_{orb} = 1.25$. The corotation radius of 5 kpc is indicated as well. For this model, Q in the initial conditions varies from 0.4 at the inner radius to 6.3 at the outer radius. The nature of the interarm features in this model is much more clear than in the corresponding model with constant Q (SMHD4, shown in Fig. 13(a)). Inside corotation, the interarm features, which are connected with the arm clumps, occur exterior to the main spiral arms. However, outside corotation, the interarm sheared features emanate inwards from the main arms in the opposite sense from those inside corotation. This direction is downstream from the arms, as seen in a frame rotating at Ω_p. Near corotation, clumps in the arms exist, but do not extend much either interior or exterior to the arms.

5.   Analysis and Discussion

5.1.   Arm Spurs or Sheared Background Features?

In our presentation and description of the models in §4, we have referred to the interarm structures we identify as features, not spurs. We will define spurs as interarm features that are distinctly associated with spiral arms, intersecting the main spiral arms at locations where self-gravity caused the growth of clumps. Using this definition, spurs in the present global models would therefore be analogies of the structures studied in the local models of KO.

Of course, it is well known that self-gravitating instabilities grow when the surface density is large enough, whether or not there is an external potential. The resulting over-dense entities, which grow via swing amplification, are stretched due to the shear in the disk. The interarm features arising in our models with spiral perturbations have similar shapes to those in the stability test models, since the interarm shear profile is similar to that of the unperturbed velocity field. At first glance, it is therefore not obvious whether the interarm features in the spiral models are specifically due to the spiral perturbation, or whether they would arise regardless of the presence of the spiral perturbation.

Given, however, the dependence of the orientation of dense interarm features on the spiral pattern speed (or the corotation radius) as seen in Figures 13(a) and 15, it is clear the external potential can have a significant effect. Depending on whether the spiral potential sweeps through the gas (outside corotation), or whether the gas overtakes the spiral potential (inside corotation), the interarm features in these cases grow inward or outward from the arm, respectively. This reversal of orientation indicates that the growth of such features is dependent on the spiral potential. These dense features, furthermore, are all connected to distinct arm clumps; they therefore fit our definition of "true spurs." On the other hand, the lower density interarm features evident in Figures 8(b) and 12(b) are similar to the structures seen in Figure 6 that grow in the absence of a spiral potential, provided the interarm surface density is sufficiently high. These "background features" are often *not* associated with arm clumps when they are present; we therefore do not consider them "true spurs."

We can quantify the effect of the spiral potential on outer-disk features by computing the dimensionless wavenumber of the background features $K_{y,feature} = \lambda_J/\lambda_{feature}$. Here, $\lambda_J = c_s^2/(G\Sigma)$ is the local two-dimensional Jeans length, and $\lambda_{feature}$ is the mean azimuthal separation of the background features. Table 3 shows the feature separation and the wavenumber for MHD models ($\beta = 1$) with the external potential strengths F = 0%, 1%, 3%, and 10%, for a region in the outer part of the disk. The other parameters are the same as the fiducial model: $i = 10°$, $\Omega_p = 8.4$ km s^{-1} kpc^{-1}, and $Q_0 = 2$ (with initial surface density

distribution $\propto R^{-1}$). For the feature separation $\lambda_{feature}$, we use the mean of the distances between the peaks of the interarm features at a radius of $R = 9.9$ kpc, along an arc of $80°$, at $t/t_{orb} = 1$ (the feature separation does not vary much with time). At $R = 9.9$ kpc, using the initial surface density we find $\lambda_J = 1.4$ kpc. The table shows that the feature separation does not vary much with the strength of the external potential, suggesting that these outer-disk features are not "true spurs." In fact, the feature separation is always approximately the Jeans length. For model SMHD3 ($Q_0 = 1$, $F = 10\%$), the feature separation at the same radius is 1.2 kpc. The value of λ_J is half that of the $Q_0 = 2$ model, while the feature spacing decreases by 30%. This gives a ratio $K_{y,feature}$ that is $\approx 30\%$ smaller when $Q = 1$ than when $Q = 2$, but is still close to unity.

From Figure 9, it is clear that a strong external potential is required for interarm features to grow in the inner regions. Similarly, in $Q \propto R$ models (Fig. 14), stretched interarm features only grow near the arms in models with a strong external potential. In models having $Q \propto R$ without an externally imposed spiral potential (Fig. 7(b)), sheared trailing features do not grow in the inner regions. Further, the features that do grow in models with strong spiral potentials are connected to the clumps that form in the spiral arm itself. Thus, we identify the interarm features in the inner regions as true arm spurs, and for measuring the separation we replace the symbol $\lambda_{feature}$ by λ_{spur}. At $R \approx 4.5$ kpc, we measure values of $\lambda_{spur} \approx 0.6$ kpc, and $\lambda_J \approx 0.6$ kpc using the initial surface density. We find that the spur separation is again approximately equal to the Jeans length at ambient densities. If instead we had used the value of Σ in the arm, λ_J would decrease, giving the ratio $\lambda_{spur}/\lambda_{J,arm} \sim$ 5.[3] For model SMHD3 ($Q_0 = 1$), both λ_{spur} and the arm surface density (therefore $\lambda_{J,arm}$) are comparable to those quantities in model SMHD2, though the initial background surface densities differ by a factor of two. Thus, for $Q = 1$ the ratio $\lambda_{spur}/\lambda_{J,background} \approx 2$, and $\lambda_{spur}/\lambda_{J,arm} \approx 5$. Evidently, for "true spurs" the spacing depends more directly on $\lambda_{J,arm}$ than on $\lambda_{J,background}$. Even though spurs will grow in the inner regions only if there is a strong spiral potential, the distance between the spurs is still within a factor of two of the minimum scale length required for gravitational instability under uniform conditions; when $Q = 2$ the ratio $\lambda_{spur}/\lambda_{J,background}$ is indistinguishable from the case of "background features" that grow in the outer regions independent of the spiral potential. For realistic Q values near 2, the separation of filamentary structures is thus not sufficient in itself to determine their origin. The additional consideration of whether structures are connected to arm clumps or not discriminate between "true spurs" and swing-amplified "background features."

---

[3]In this region, $\Delta R \sim 25$ pc and $R\Delta\theta \sim 15$ pc, so the Jeans length using arm densities is resolved.

5.2. Spurs and Arm Clumps

As discussed above, we term interarm features that grow out of arm condensations "true spurs." When interarm features grow as background effects, strong condensations can also grow within and remain in the arm. In this case, however, there is not a one-to-one relationship between interarm features and arm condensations (see e.g. the outer regions of Fig. 8(d) and Fig. 12(a)). In both situations, however, the arm condensations that grow are generally regularly spaced, similar to the "beads on a string" of bright HII regions often observed in spiral galaxies. The spacings between the clumps in the $Q_0 = 2$ model (SMHD2) at $R \approx 4.5$ kpc is typically $\sim$630 pc, comparable to $5\lambda_{J,arm}$ (measured using arm surface densities before fragmentation). In other models with distinct arm clumps, such as SMHD3 ($Q_0 = 1$), SMHD4 ($R_{CR} = 5$ kpc) and SMHD5 ($i = 20°$) we measure clump spacings of $\sim$3 - $5\lambda_{J,arm}$.

We also measured the width W of the spiral arms. For the fiducial model SMHD2 ($Q_0 = 2$ and $F = 10\%$), the FWHM $W \approx 210$ pc, for the same region of the arm for which the clump/spur spacing was measured. The ratio $\lambda_{spur}/W \sim 3$ is consistent with the observational study of Elmegreen & Elmegreen (1983) and the theoretical analysis of Elmegreen (1994). For the $Q_0 = 1$ model, SMHD3, we measure an arm width $W \approx 600$ pc, and clump/spur spacing of ≈ 600 pc. Thus, when $Q_0 = 1$ the ratio λ_{spur}/W is close to unity. The measured ratio $\lambda_{spur}/\lambda_{J,arm}$ is therefore more consistent between our differing Q models than the ratio λ_{spur}/W, possibly due to magnetic fields and the physics of MJI (see KO). In practice, however, the observed range of Q might not be large enough to distinguish a difference.

For models shown in Figure 8 (and 9), only model SMHD2, with a strong spiral potential, shows distinct clumps in the arms. In the case with a weaker potential, the density transitions smoothly from the arm to the interarm features. Using the clump finding algorithm `clumpfind` (Williams et al. 1994), we consistently measure the clump masses to be $M_{cl} \approx 10^7 M_\odot$ in the arms of model SMHD2. In terms of the Jeans mass

$$M_J = \frac{c_s^4}{G^2 \Sigma} \tag{12}$$

$M_{cl} \approx 10 M_J$ using mean arm surface densities. We measure similar values for the other models with distinct arm clumps. We find that altering the contour levels for the clump finding algorithm does not significantly change the total mass of clumps, but only increases the number of clumps found, giving similar masses for the new clumps. For models with weaker spiral potentials, strong clumps are not found in the spiral arms, so we cannot define clumps in the arm as easily; as discussed, the interarm features in models with weak potentials are not true arm spurs.

In observations of many galaxies, especially the HST and Spitzer images of M51, and other galaxies in the SINGS sample (Scoville & Rector 2001, and Kennicutt et al. 2003), the strong interarm features indeed tend to intersect the brightest regions in CO along the main dust lanes (La Vigne et al. 2006). Vogel, Kulkarni, & Scoville (1988) found molecular complexes with masses of $10^7 - 10^8 M_\odot$ in M51, which they named Giant Molecular Associations (GMAs). In spiral galaxies for which the gaseous component is not predominantly molecular, large HI clouds have also been found to have masses of $\sim 10^7 M_\odot$; these are termed "superclouds" by Elmegreen & Elmegreen (1983). Both the GMAs and superclouds are analogous to the arm clumps in our simulations, which do not include the chemistry of the gas. In addition, La Vigne et al. (2006) measure feather spacings of ~ 7 - $11\lambda_J$ in M51 and $\sim 1.5\lambda_J$ in NGC 0628, using surface densities in the arm to compute λ_J. These measurements assume the same value of c_s for both cases, and may be affected by uncertainty in the conversion of CO luminosity to gas mass. The consistency of clump masses and spur separations and the clump/spur connection in our models to the GMA masses, interarm feather separations, and GMA/feather association in M51 suggests that the strong spiral potential is directly responsible for producing these structures.

The orientation of spiral arm spurs indicates whether a given region is inside or outside corotation. Thus, the location of corotation can be identified if the transition from inward to outward directed spurs is observed. As discussed in KO, however, there are presently no known galaxies that exhibit clear inward projected spurs for a number of possible reasons, such as relatively weaker arms outside corotation, and current resolution limits.

5.3. Offset between Gaseous Arm and Potential Minimum

As indicated in §3, the relative location between the gaseous arm peak and the minimum in the spiral potential varies depending on the strength of the potential and the corotation radius. Figure 16 shows the azimuthal locations of these peaks, which would be observed as the main dust lanes, for three models relative to the potential minimum, as a function of radius. The location of the potential minimum for models HD1 and HD2 at any given time is the same; only the strength of the potential differs. Inside corotation, the gaseous arms from models (including those not shown here) with stronger potentials form closer to, though always downstream from, the potential minimum. As shown in Figure 16(b), the gaseous arm shifts from downstream to upstream from the potential minimum at corotation.

Gittins and Clarke (2004), hereafter GC, find via the one-dimensional shock-fitting procedure of Shu, Milione, & Roberts (1973) with local non-self-gravitating models, that the gas shock occurs upstream from the potential minimum. The magnitude of the offset

depends on various parameters. They find that this offset approaches $-\pi$ at corotation, suggesting that the location of corotation can be constrained by measuring offsets between the arm in K band (tracing the potential) and molecular (gas) observations. In the cases studied by GC, the potential minima and the gaseous shock intersect well inside corotation. The location of this intersection varies depending on the strength of the spiral potential.

There are a number of possible reasons for the differences in offsets between our models and the results of GC. Perhaps most importantly, we use a flat rotation curve, whereas GC uses a velocity profile that varies with radius. In addition, we measure the position of the density peak (shocks are difficult to distinguish near corotation at our resolution) while GC report on the position of the shock, which may be upstream from the density peak. Such differences between the parameters and analysis methods in our models and those of GC prevent a direct comparison of the results. We note that both studies include the effect of the stellar disk only as a fixed rotating spiral potential, i.e. an unresponsive component. The relative locations of the gaseous and stellar arms may well depend on the mutual self-consistent interaction between the two components, an important issue for future investigation.

5.4. Effect of Disk Thickness on Stability

In our calculation of the gaseous self-gravity, we (approximately) include the effect of disk thickness H (see Appendix). Including this disk thickness approximation, the local axisymmetric dispersion relation for an unmagnetized medium becomes:

$$\omega^2 = \kappa^2 + c_s^2 k^2 - \frac{2\pi G\Sigma|k|}{1 + |k|H}. \tag{13}$$

When $H = 0$, the dispersion relation takes on its familiar form for razor thin disks (e.g. Binney & Tremaine 1987). In order to solve for the minimum value of ω, we define

$$k_0 \equiv \frac{\pi G\Sigma}{c_s^2} = \frac{\kappa}{Qc_s}, \tag{14}$$

and

$$y \equiv k/k_0, \tag{15}$$

so that at ω_{min},

$$y(1 + k_0 Hy)^2 = 1. \tag{16}$$

The critical value of Q (where $\omega_{min}^2 = 0$) is then given by

$$Q_{crit}^2 + y^2 - \frac{2yQ_{crit}}{Q_{crit} + y(\frac{\kappa H}{c_s})} = 0. \tag{17}$$

We solve equations (16) and (17) simultaneously, and Figure 17 shows how Q/Q_{crit} varies with R, for disks with $Q = 2$. With the modified dispersion relation of equation (13), and $H = $ constant, disk stability decreases with increasing R. As shown in Figure 17, in the inner regions disks with large values of H are much more stable than razor thin disks, for which $Q_{crit} = 1$ (Toomre 1964).

The stability profile for axisymmetric perturbations will also influence the stability of non-axisymmetric perturbations (e.g. Goldreich & Lynden-Bell 1965, Toomre 1981, and Kim & Ostriker 2001). As seen in Figure 6, the outer regions of constant Q, constant H disks are unstable. The maximum radius of the inner stable region, R_{crit}, depends on Q, and is constant in time. Models with varying thicknesses show that R_{crit} increases with larger values of H, qualitatively consistent with the stability profiles in Figure 17. We note that R_{crit} in our models with different values of H does not simply correspond to $Q/Q_{crit} = $ constant, however. For example, with $H = 25$ pc, we measure $R_{crit} = 5.2$ kpc empirically, and Q/Q_{crit} $= 2.4$ at this location. On the other hand, for $H = 200$ pc, we measure $R_{crit} = 7.8$ pc, and $Q/Q_{crit} = 3.7$ at this location. Thus, the value of Q obtained from a modified dispersion relation (including the effect of thickness) is not sufficient for a complete characterization of non-axisymmetric stability limits in global models.

We also find that in models with smaller values of H, the instabilities (outside R_{crit}) grow sooner than in models with larger values of H. Further, the spacing between the perturbations also vary if H is altered significantly. We find that increasing H by a factor of 8 increases the perturbation separation by a factor of ~ 2.5. Slightly varying the thickness does not strongly affect the perturbation spacing, however. We also note that in our implementation $H = $ constant, which favors structures to grow in the outer regions; other choices of the thickness profiles, such as $H/R = $ constant, can result in stable outer regions combined with unstable inner regions.

6.   Summary

We have investigated the growth of interarm features in self-gravitating gaseous disks of spiral galaxies using global MHD simulations. Our models are two-dimensional, but we account for the thickness of the disk in an approximate way in the computation of self-gravity. Gaseous spiral arms grow as a result of an externally-imposed rotating spiral potential, representing the stellar spiral arms of a galaxy. We explore a range of values for the physical parameters describing the properties of the disk. The main results are as follows:

1) In the inner regions of disks without self-gravity or magnetic fields, we are able to

reproduce the interarm features that WK found in their models. When spiral shocks are strong enough, hydrodynamic instabilities cause the growth of knots in the spiral arms, and the shear causes interarm features to spread from these knots. However, we find that inclusion of magnetic fields gives more tensile strength to the spiral arms, and suppresses the growth of such features.

2) In disks with a low amplitude (external) spiral potential but without self-gravity, our simulations show long lasting spiral patterns in the gas. We also obtain bifurcation features (arm branches) near locations of Lindblad and ultraharmonic resonances, similar to features discussed in CLS.

3) To assess the intrinsic stability of disks for growth of moderate ($\sim$kpc) scale structure, we simulated self-gravitating disks without an external spiral potential. Slightly over-dense regions (nonlinearly) grow in density due to self-gravity, and subsequently become stretched due to the rotational shear. For disks with a constant Toomre parameter Q (equivalently, with initial surface density distribution $\propto R^{-1}$) and thickness H, the instability initially grows in the outermost regions. Only the inner regions remain stable. For disks with a lower value of Q_0, the size of the inner stable region decreases, and the instabilities grow sooner. As the thickness of the disk decreases, so does the size of the inner stable region.

4) In self-gravitating disk models with an external spiral potential, interarm feather-like features can arise in two distinct ways. One way these features can develop is essentially the same as in models without spiral structure summarized in (3) above, i.e. via swing amplification in the interarm region. Stronger spiral potentials changes the spacing of these features only slightly. However, strong spiral potentials can lead to growth of self-gravitating knots strung out as beads along the arms. Growing arm condensations in turn can produce interarm feathering in a second way, by concentrating gas as it flows from the arm into the interarm regions. If we define "true spurs" as distinct interarm features associated with the brightest regions in the arm, these structures only form in self-gravitating disks with strong ($F \approx 10\%$) external potentials.

5) Bound clumps that grow in the spiral arms have masses of $\sim 10^7 M_\odot$. The spacings of these clumps, or equivalently, spurs, are measured to be $\sim$3 - $5\lambda_{J,arm}$. In models where $Q_0 = 2$, the ratio of clump spacing to arm width is consistent with the prediction $\lambda/W \approx 3$ from Elmegreen (1994) and the observational study of Elmegreen & Elmegreen (1983). In many galaxies large clouds, such as GMAs and superclouds, are observed to have similar masses and spacings to the knots in our models.

6) We find that without magnetic fields, the arms in self-gravitating models rapidly fragment, destroying the continuous, distinct spiral arm shape. Thus, magnetic fields may

be important for maintaining the integrity of grand design spiral structure in the ISM, even as self-gravity (and star formation) work to destroy these large-scale patterns.

7) The distribution and extent of interarm features that grow in self-gravitating models depend on the surface density distribution (or, equivalently, the instability parameter Q). For R^{-1} surface density distributions, for which Q is initially constant, strong feathering grows early on in the outer regions of the disk. At later times in the inner regions, spurs grow from the arm clumps and extend out to nearly the adjacent arm. For R^{-2} surface density distributions, Q increases with radius. For these disks, spur formation in the outer regions is suppressed, but prominent spurs still grow in the inner regions. Our models have adopted $H = $ constant; if H increases with R, it is possible to have inner-disk instability and outer-disk stability even with $Q = $ constant.

8) The orientation of the spurs with respect to the arms depends on the pattern speed of the spiral potential. Inside corotation, spurs extend outward from the convex side of the main dust lanes, as this is the downstream side of the arm. Outside corotation, the potential rotates faster than the gas, so the spurs form inside the main dust lanes. In principle, a reversal in the orientation of spurs in observed galaxies could be used to determine the position of the corotation radius.

Though we were able to produce spurs and quantify the conditions necessary for the growth of spurs with the models of this work, we were unable to follow the subsequent evolution of the disk for many orbits. Runaway growth of the massive clumps in the spiral arms causes the surrounding gas to have large velocities, which implies short timesteps in order to satisfy the Courant condition. In addition, the densities become sufficiently large and the clumps so small that they are not well resolved by our grid. However, the physicality of the simulation itself can be questioned at late times, because real condensations would not grow uninhibited. The agglomeration of gas in galaxies into GMCs eventually leads to the formation of stars. The photoionization and mechanical inputs from HII regions and supernovae associated with massive star formation in GMCs returns much of their gas to the diffuse phase. In future work, we plan to implement feedback mechanisms, using appropriate energy injection rates from typical star formation processes to disperse the clumps formed in the arms. We also plan to include heating and cooling processes to simulate a realistic multi-phase medium. By including processes of this kind, it will be possible to study the spur structure morphology and GMC formation rates and properties consistent with quasi-steady-state conditions.

A.   Appendix

A.1.   Self-Gravity: Cartesian Coordinates

Numerically, Poisson's Equation

$$\nabla^2\Phi = 4\pi G\rho, \tag{A1}$$

can be solved efficiently using Fourier methods. In 3D Cartesian coordinates,

$$\hat{\Phi}(k_x, k_y, k_z) = -\frac{4\pi G\hat{\rho}(k_x, k_y, k_z)}{k^2}, \tag{A2}$$

where $\hat{\Phi}$ and $\hat{\rho}$ are the Fourier transform of the potential Φ and density ρ, and $k^2 = k_x^2 + k_y^2 + k_z^2$. With density periodic on a domain (L_x, L_y, L_z) with (N_x, N_y, N_z) zones in each dimension, respectively, the values of $k_x = \pm n_x 2\pi/L_x$ with $n_x = 1 \ldots N_x/2$.

For an infinitesimally thin, two dimensional disk, one may use separation of variables to show that the potential within the disk in Cartesian coordinates satisfies

$$\hat{\Phi}(k_x, k_y) = -\frac{2\pi G\hat{\Sigma}(k_x, k_y)}{|\mathbf{k}|}, \tag{A3}$$

where $\hat{\Sigma}$ is the Fourier transform of the surface density Σ (e.g. Binney & Tremaine 1987) . The effect of the nonzero disk thickness may be accounted for in an approximate way (Kim, Ostriker, & Stone 2002), such that equation (A3) becomes

$$\hat{\Phi}(k_x, k_y) = -\frac{2\pi G\hat{\Sigma}}{|\mathbf{k}|(1 + |\mathbf{k}|H)}, \tag{A4}$$

where H is the thickness of the disk, and $\Sigma = 2H\rho$.

Obtaining the potential using Fourier methods expressed in equations (A2) or (A3) assumes that the density is periodic. Thus, the resulting potential includes a contribution from replicas of the density distribution (outside the computational domain). If in fact one desires to compute the potential of a spatially isolated system with zero density outside of the computational domain, then this method is modified by computing Fourier transforms on

a larger, zero-padded array. The central portion of the larger array is filled with the density values from the original domain, and the surrounding zones are set to zero. For obtaining a solution of the Poisson's equation the zero-padded array must be at least twice the size of the original array in each dimension (e.g. Hockney & Eastwood 1981). A larger padded region moves unphysical cusps away from the boundaries of the computational domain; of course, increasing the size of the padded region requires more memory as well as CPU time.

A.2. Self-Gravity: Polar Coordinates

In 2D cylindrical polar coordinates, a number of techniques have been explored to calculate the potential. Miller (1978) describes a method which sums the potential due to concentric rings in polar coordinates. The potential at (R, ϕ) is written as

$$\Phi(R, \phi) = -G \int_0^\infty R' \, dR' \int_0^{2\pi} d\phi' \, D(R, R'; \phi - \phi') \Sigma(R', \phi') \tag{A5}$$

where

$$D(R, R'; \phi - \phi') = (R^2 + R'^2 + \epsilon^2 - 2RR' \cos(\phi - \phi'))^{-\frac{1}{2}}. \tag{A6}$$

Here, ϵ is a softening parameter. We can discretize equation (A5), writing the result as

$$\Phi(R_i, \phi_l) = -G \sum_n \sum_j D(R_i, R_j; \phi_l - \phi_n) \Sigma(R_j, \phi_n) \delta A_{jn} \tag{A7}$$

where $\delta A_{jn} = R_j \delta R_j \delta \phi_n$. The direct summation in equation (A7) is computationally expensive; however, Fourier transforms can accelerate the computation. The integral over ϕ' in equation (A5) is a convolution of D with the mass distribution in the ring at R_j' with the equivalent for the sum in equation (A7). By the Fourier convolution theorem, we can write

$$\hat{\Phi}_n(R_i) = -G \sum_{R_j} \hat{D}_n(R_i, R_j) \hat{M}_n(R_j), \tag{A8}$$

where $\hat{M}_n(R_j)$ is the 1D Fourier transform in the azimuthal direction of the mass $M_{j,n} = \Sigma_{j,n} \delta A_{j,n}$. The discrete Fourier transform (in the $\hat{\phi}$ direction) of the Green's Function $D(R, R'; \phi - \phi')$, $\hat{D}_n(R_i, R_j)$, only needs to be computed once, at the beginning of the simulation. For an (R, ϕ) computational grid, including periodic replicas of the density is required to cover the full 2π domain of the azimuthal coordinate. The computational domain must therefore be $2\pi/m$ for some m; we use $m = 2$ for a two-armed spiral. Aside from the effect of softening, this method of computing the potential is exact.

Even though Miller's (1978) method is more efficient than direct summation of equation (A7), more memory and CPU time are still required than for a pure Fourier approach. Thus,

for numerical expediency, we instead use a computationally more efficient method to obtain an approximate solution for Φ. Though this method is not an exact calculation of Φ, we will show that the differences between the exact (Miller) method and our more efficient method is small. After describing our method, we will show how the results, as well as CPU usage, from the different methods compare.

To compute an approximate potential Φ in polar coordinates based solely on Fourier transforms, we make use of the method described in §A.1. We will hereafter refer to this method as the coordinate transformation method. If we apply a coordinate transformation

$$
\begin{aligned}
x &\equiv R_0 \ln\left(\frac{R}{R_0}\right) \\
y &\equiv R_0 \phi,
\end{aligned}
\tag{A9}
$$

Poisson's equation becomes

$$
\frac{\partial^2 \Phi}{\partial x^2} + \frac{\partial^2 \Phi}{\partial y^2} + \left(\frac{R}{R_0}\right)^2 \frac{\partial^2 \Phi}{\partial z^2} = \left(\frac{R}{R_0}\right)^2 4\pi G\rho.
\tag{A10}
$$

For in-plane gradients large compared to vertical gradients, the solution is

$$
\hat{\Phi}(k_x, k_y) = -\frac{2\pi G\hat{\tilde{\Sigma}}}{|k|^2 H},
\tag{A11}
$$

where $\tilde{\Sigma} = (R/R_0)^2 \Sigma$. This has the same form as equation (A4) in the limit $|k|H \gg 1$.

More generally, solutions to the Laplace equation in cylindrical coordinates have the form $\sum_{k,l} A_{kl} C_l(kR) e^{il\phi} e^{-|kz|}$ where the C_l's are two independent Bessel functions - e.g. J_l and Y_l - and where $|z| \to \infty$ and azimuthal boundary conditions have been applied. The coefficients of each term in the sum is determined by the requirement that $\partial\Phi/\partial z|_{z=0^+} = 2\pi G\Sigma(R, \phi)$. Each A_{kl} can then be written as a Fourier-Hankel transform of the surface density $A_{kl} \propto \int_0^{2\pi} e^{-il\phi} d\phi \int_{-\infty}^{\infty} dR J_l(kR) R^2 \Sigma(R, \phi)$ (e.g. Binney & Tremaine, 1987).

Since the force is dominated by terms with large gradients, the large k values are most important. For large arguments, the Bessel functions approach sinusoidal functions, so that the A_{kl}'s can be written as two-dimensional Fourier transforms of $\tilde{\Sigma}$. In this limit, we must have $\hat{\Phi}(k_x, k_y) = -2\pi G\hat{\tilde{\Sigma}}/|\mathbf{k}|$. Altogether, we may therefore write our approximate solution as

$$
\hat{\Phi}(k_x, k_y) = -\frac{2\pi G\hat{\tilde{\Sigma}}}{|\mathbf{k}|(1 + |\mathbf{k}|H)},
\tag{A12}
$$

Here, $k_y = l/R$ and k_x is the wavenumber corresponding to the transformed radial coordinate. In order to have the x_i values equally spaced, the radial grid coordinates are equally separated in $\log R$.

With this method, the surface density is implicitly assumed periodic in both azimuth and radius. The spurious contribution from periodic replicas in the radial direction can be minimized by zero padding the edges of the density array in the radial direction, as described at the end of §A.1.

A.3. Comparison of Methods

To compare the effects of the periodic replicas in the test cases for the coordinate transformation method, we use arrays that are $2\times$, $4\times$, $8\times$, $16\times$, and $32\times$ the size of the original density array. The computational domain for the comparison tests has 256 radial elements and 1024 azimuthal elements. As an example, for the case for which we use a $4\times$ larger array, the size of the $\tilde{\Sigma}$ array before taking a Fourier transform to obtain $\hat{\tilde{\Sigma}}$ is 1024×1024. The actual values of the densities are stored in array elements where the first (radial) index is between 385 and 640. All other elements of the array are set to zero.

To compare the two methods of computing the potential from test simulations, we arrange test cases for which the total mass in the computational domain is 0 or very small. The Fourier method will include contributions from matter outside the computational domain, due to the assumed periodicity of the density. Thus, minimizing the total mass will reduce this superfluous contribution. In analyzing the differences between the methods, we keep in mind that the softening will affect the numerical values of the potential (and force) in regions with large density gradients. With the coordinate transformation method, we also compare the results from cases where the size of the zero padded zones vary.

We inspect the potential of three test disks containing (1) a positive and negative ring, (2) a positive and negative radial spoke, and (3) and a positive and negative logarithmic spiral arm. We compare the region in between the positive and negative mass distributions regions, to avoid edge effects. For test cases (1) and (2), we find the relative difference between the coordinate transformation and the Miller method ($|\Phi_{CT} - \Phi_{MM}|/\Phi_{MM}$) to be within $\sim 3\%$. For test case (3), we measure a relative difference of $\sim 5\%$. Again, these relative differences are measured between the positive and negative density regions, away from the edges of the disk. For the self-gravitating simulations we perform, we are interested in the growth of substructures under similar circumstances, i.e. away from the edges of the disk, near regions where the perturbed density is both positive and negative. Nevertheless, even near the edges, all tests give values of the potential that agree within $\sim 25\%$. Finally, the difference between the tests using the coordinate transformation (with varying sizes of the zero-padded zone) is negligible.

The main advantage of using the coordinate transformation method is the decrease in CPU time for each simulation. For this method computing the potential requires a multiplication of the density to obtain $\tilde{\Sigma}$, a Fourier transform to obtain $\hat{\tilde{\Sigma}}$, a multiplication in Fourier space for the gravitational kernel in equation A12, and an inverse Fourier transform to obtain Φ. This sequence requires fewer operations than the Miller computational method.

To measure the efficiency of each method, we use a slightly different test simulation from the ones described above. In these tests, with a grid of 256 radial and 512 azimuthal zones, a spiral potential is turned on over the first half orbit, then the self-gravitational potential is slowly turned on over another half an orbit. Thus, both potentials are turned on fully after 1 orbit. The test simulations are subsequently allowed to run for an additional orbit, after which the CPU times are compared.

All these tests, as well as many of the simulations presented in this paper, were run on a machine with a 2.99 GHz Pentium 4 processor, with 2 GB of RAM. Table 4 shows the CPU time (relative to that using the exact solution) required for each test to run. It is evident, as expected, that the simulations using the coordinate transformation method (where we enlarge the density array by $2\times$, $4\times$, or $8\times$) requires much less CPU time than those using the exact potential computational method. Since the numerical differences between the methods are modest, and to take advantage of the superior efficiency of the coordinate transformation method, we use the coordinate transformation method, enlarging the density array by $4\times$, for our high resolution simulations presented in this paper. We have also tested models using the Miller method, and obtain essentially the same results.

REFERENCES

Aalto, S., Hüttemeister, S., Scoville, N. Z., & Thaddeus, P. 1999, ApJ, 522, 165

Artymowicz, P., & Lubow, S. H. 1992, ApJ, 389, 129

Balbus, S. A. 1988, ApJ, 324, 60

Binney, J., & Tremaine, S. 1987, Princeton, NJ, Princeton University Press, 1987, 747 p.,

Chakrabarti, S., Laughlin, G., & Shu, F. H. 2003, ApJ, 596, 220 (CLS)

Dobbs, C. L., & Bonnell, I. A. 2006, MNRAS, 367, 873

Elmegreen, D. M. 1980, ApJ, 242, 528

Elmegreen, B. G., & Elmegreen, D. M. 1983, MNRAS, 203, 31

Elmegreen, B. G. 1994, ApJ, 433, 39

Frigo, M, & Johnson, S. G. 2005, Proceedings of the IEEE, 93, 216

Goldreich, P., & Lynden-Bell, D. 1965, MNRAS, 130, 125

Rand, R. J. 1995, AJ, 109, 2444

Gittins, D. M., & Clarke, C. J. 2004, MNRAS, 349, 909 (GC)

Hockney, R. W., & Eastwood, J. W. 1981, Computer Simulation Using Particles, New York: McGraw-Hill, 1981,

Kennicutt, R. C., et al. 2003, PASP, 115, 928

Kim, W.-T., & Ostriker, E. C. 2001, ApJ, 559, 70

Kim, W.-T., & Ostriker, E. C. 2002, ApJ, 570, 132 (KO)

Kim, W.-T., & Ostriker, E. C. 2006, ApJ Accepted, astro-ph/0603751

Kim, W.-T., Ostriker, E. C., & Stone, J. M. 2002, ApJ, 581, 1080

La Vigne, M. A., Vogel, S. N., & Ostriker, E. C., 2006 In Preparation

Lin, C. C., & Shu, F. H. 1964, ApJ, 140, 646

Lowe, S. A., Roberts, W. W., Yang, J., Bertin, G., & Lin, C. C. 1994, ApJ, 427, 184

Lynds, B. T. 1970, IAUS, 38, 26L

Martin, C. L., & Kennicutt, R. C. 2001, ApJ, 555, 301

Miller, R. H. 1976, J. Comput. Phys., 21, 400

Rand, R. J. 1993, ApJ, 410, 68

Regan, M. W., Thornley, M. D., Helfer, T. T., Sheth, K., Wong, T., Vogel, S. N., Blitz, L., & Bock, D. C.-J. 2001, ApJ, 561, 218

Roberts, W. W. 1969, ApJ, 158, 123

Scoville, N. Z., & Rector, T 2001, HST Press Release

Shetty, R., Vogel, S. N., Teuben, P. J., Ostriker, E. C., 2006 In Preparation

Shu, F. H., Milione, V., & Roberts, W. W. 1973, ApJ, 183, 819

Stone, J. M., & Norman, M. L. 1992, ApJS, 80, 753

Stone, J. M., & Norman, M. L. 1992, ApJS, 80, 791

Teuben, P. 1995, ASP Conf. Ser. 77: Astronomical Data Analysis Software and Systems IV, 77, 398

Toomre, A. 1964, ApJ, 139, 1217

Toomre, A. 1981, Structure and Evolution of Normal Galaxies, 111

Truelove, J. K., Klein, R. I., McKee, C. F., Holliman, J. H., Howell, L. H., & Greenough, J. A. 1997, ApJ, 489, L179

Visser, H. C. D. 1980, A&A, 88, 149

Vogel, S. N., Kulkarni, S. R., & Scoville, N. Z. 1988, Nature, 334, 402

Wada, K., & Koda, J. 2004, MNRAS, 349, 270 (WK)

Williams, J. P., de Geus, E. J., & Blitz, L. 1994, ApJ, 428, 693

Wong, T., & Blitz, L. 2002, ApJ, 569, 157

Table 1.   Parameters for Models Without Gas Self-Gravity

Model	β	F (%)	Ω_p (km s^{-1} kpc^{-1})	i (°)
(1)	(2)	(3)	(4)	(5)
HD1	∞	3	8.4	10
HD2	∞	10	8.4	10
HD3	∞	10	42	10
HD4	∞	10	8.4	20
MHD1	1	10	8.4	10

Table 2.   Parameters for Models Including Gas Self-Gravity

Model [a]	β	F (%)	Ω_p (km s^{-1} kpc^{-1})	i (°)	Q_0
(1)	(2)	(3)	(4)	(5)	(6)
SHDne1	∞	0	-	-	1
SHDne2	∞	0	-	-	2
SMHDne	1	0	-	-	1
SMHD1	1	3	8.4	10	2
SMHD2	1	10	8.4	10	2
SMHD3	1	10	8.4	10	1
SHD1	∞	10	8.4	10	2
SMHD4	1	10	42	10	2
SMHD5	1	10	8.4	20	2

[a]Models listed in the text with a prime (e.g. SHDne1′) have $\Sigma \propto R^{-2}$; otherwise, $\Sigma \propto R^{-1}$

Fig. 1.— Snapshots from non self-gravitating, unmagnetized model HD1 (weak external spiral potential, $F = 3\%$). Surface density at (a) $t/t_{orb} = 1$, when the external potential is turned on fully, (b) $t/t_{orb} = 2$, and (c) $t/t_{orb} = 3$. (d) Inner 6.8×6.8 kpc^2 box shown in (c). Color scale for (a), (b), and (c) is shown above (a) and (b), in units of $\log(\Sigma/\Sigma_0)$. Color scale for (d) is shown adjacent to (d), in units of Σ/Σ_0.

Table 3. Scale of Interarm Features

F [a]	$\lambda_{feature}$ [b]	$K_{y,feature}$ [c]
0	1.3	1.1
1%	1.3	1.1
3%	1.4	1.0
10%	1.7	0.8

[a]External Potential Strength

[b]Feature separation (kpc)

[c]$\lambda_J/\lambda_{feature}$; $\lambda_J = 1.4$ kpc

Table 4. CPU Time for Different Potential Computation Methods

CT (2×) [a]	CT (4×) [a]	CT (8×) [a]	CT (16×) [a]	CT (32×) [a]	MM [b]
0.59	0.62	0.70	0.89	1.25	1.0

[a]CT: Coordinate Transformation, with zero-padded enlargement of density array as indicated in parentheses

[b]MM: Miller's Method

Fig. 2.— Snapshots from non self-gravitating, unmagnetized model HD2 (strong external spiral potential, $F = 10\%$). Surface density at (a) $t/t_{orb} = 1$, when the external potential is turned on fully, (b) $t/t_{orb} = 2$, and (c) $t/t_{orb} = 3$. (d) Inner 6.8×6.8 kpc^2 box shown in (c). Color scales are arranged in the same manner as in Figure 1.

Fig. 3.— Snapshots at $t/t_{orb} = 2$, from models HD3 (a) and HD4 (b). Parameters are the same as in model HD2 (Fig. 2), but with (a) $\Omega_p = 42$ km s^{-1} kpc^{-1}, and (b) $i = 20°$. The dashed circle in (a) indicates the corotation radius of 5 kpc. Color scale shows $\log(\Sigma/\Sigma_0)$.
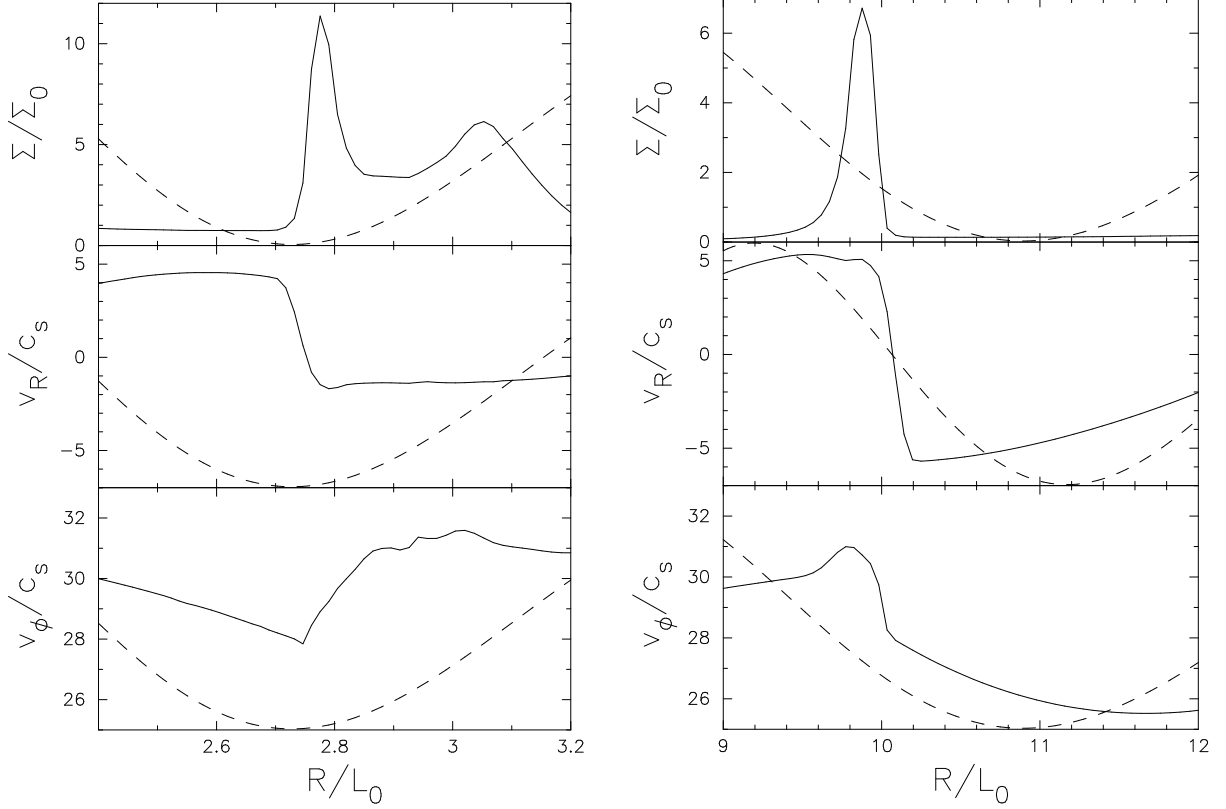
Fig. 4.— Density, radial, and tangential velocity as a function of radius from model HD3 (shown in Fig. 3(a)), at time $t/t_{orb} = 1.26$. Quantities are taken from locations of constant azimuth, from a region inside corotation (left), and a region outside corotation (right). The corotation radius is $R_{CR}/L_0 = 5$. The dashed line in each plot shows the external spiral potential.

Fig. 5.— Snapshots at $t/t_{orb} = 2$ of the inner 6.8×6.8 kpc^2 of model (a) HD2 and (b) MHD1. Color scale is in units of Σ/Σ_0.

Fig. 6.— Snapshots of models with self-gravity but no external potential. (a) SHDne1 ($Q_0 = 1$) at $t/t_{orb} = 0.97$, (b) SHDne2 ($Q_0 = 2$) at $t/t_{orb} = 0.97$, (c) SMHDne ($Q_0 = 1$, $\beta = 1$) at $t/t_{orb} = 0.97$, and (d) SHDne2 ($Q_0 = 2$) at $t/t_{orb} = 1.49$. Color scale is in units of $\log(\Sigma/\Sigma_0)$.

Fig. 7.— Snapshots at $t/t_{orb} = 1.0$ of models with $Q \propto R$; (a) SHDne1′ ($Q_0 = 1$) and (b) SHDne2′ ($Q_0 = 2$). Color scale shows $\log(\Sigma/\Sigma_0)$.

Fig. 8.— Models SMHD1 ($F = 3\%$) and SMHD2 ($F = 10\%$). SMHD1 at (a) $t/t_{orb} = 1.0$ and (b) $t/t_{orb} = 1.125$. SMHD2 at (c) $t/t_{orb} = 1$ and (d) $t/t_{orb} = 1.125$. The boxed regions in (b) and (d) are the inner 14×14 kpc^2 shown in detail in Figure 9. Units of color scale are $\log(\Sigma/\Sigma_0)$.

Fig. 9.— Inner 14×14 kpc^2 of Figure 8(b) and 8(d). (a) Detail of $F = 3\%$ model from box shown in Figure 8(b), and (b) detail of $F = 10\%$ model from box shown in Figure 8(d). Color scale shows Σ/Σ_0. The boxed region in (b) is shown in Figure 10.

Fig. 10.— Boxed region from Figure 9(b) (Model SMHD2). Solid vectors show the instantaneous gas velocity in the frame rotating with the spiral potential ($\Omega_p = 8.4$ km s^{-1} kpc^{-1}, $R_{CR} = 25$ kpc). Dotted vectors show the initial velocities (pure circular motion). Scale of the vectors is shown by the thick vector (top right). Contours show magnetic field lines.

Fig. 11.— Model SHD1 ($F = 10\%$, $\beta = \infty$) at (a) $t/t_{orb} = 1.0$, and (b) $t/t_{orb} = 1.125$. Color scale is in units of $\log(\Sigma/\Sigma_0)$.

Fig. 12.— Model SMHD3 ($F = 10\%$, $Q=1$) at (a) $t/t_{orb} = 0.75$, and (b) $t/t_{orb} = 1.0$. Color scale shows $\log(\Sigma/\Sigma_0)$.

Fig. 13.— Snapshots at $t/t_{orb} = 1$ of model (a) SMHD4 ($F = 10\%$, $\Omega_p = 42$ km s^{-1} kpc^{-1}), with the corotation radius indicated by the dashed circle, and (b) SMHD5 ($F = 10\%$, $i = 20°$). Units of color scale are $\log(\Sigma/\Sigma_0)$.

Fig. 14.— Snapshot of (a) SMHD3′ ($Q_0 = 1$, $F = 10\%$) at $t/t_{orb} = 0.875$ and (c) SMHD2′ ($Q_0 = 2$, $F = 10\%$) at $t/t_{orb} = 1.125$, along with the inner 14×14 kpc of each snapshot in (b) and (d). Color scales of (a) and (c) are in units of $\log(\Sigma/\Sigma_0)$, and scales for (b) and (c) are shown in units of Σ/Σ_0.

Fig. 15.— Snapshot of model SMHD4′ ($\Omega_p = 42$ km s^{-1} kpc^{-1}) at $t/t_{orb} = 1.25$. The corotation radius is indicated by the dashed circle. Color scale is in units of Σ/Σ_0.
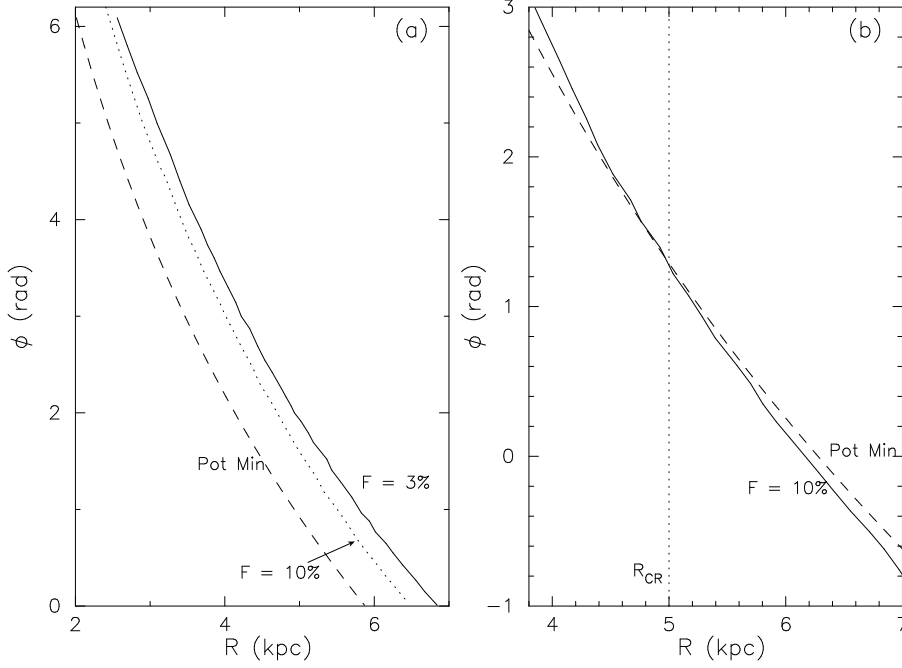

Fig. 16.— Location of potential minimum and gaseous arm peaks. (a) Models HD1 and HD2 with $F = 3\%$ and 10%, respectively, and (b) model HD3, with $F = 10\%$ and $R_{CR} = 5$ kpc.
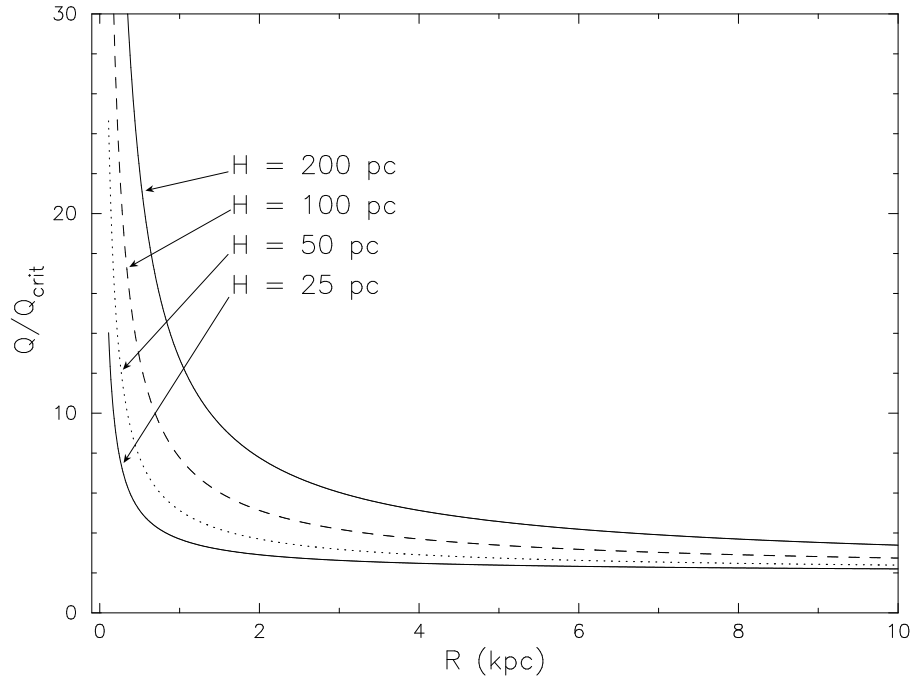
Fig. 17.— Q/Q_{crit} for $Q = 2$ models when disk thickness is included (see eqns. [13] - [16]).

This figure "f1.jpg" is available in "jpg" format from:

http://arXiv.org/ps/astro-ph/0605142v1

This figure "f2.jpg" is available in "jpg" format from:

http://arXiv.org/ps/astro-ph/0605142v1

This figure "f3.jpg" is available in "jpg" format from:

http://arXiv.org/ps/astro-ph/0605142v1

This figure "f5.jpg" is available in "jpg" format from:

http://arXiv.org/ps/astro-ph/0605142v1

This figure "f6.jpg" is available in "jpg" format from:

http://arXiv.org/ps/astro-ph/0605142v1

This figure "f7.jpg" is available in "jpg" format from:

http://arXiv.org/ps/astro-ph/0605142v1

This figure "f8.jpg" is available in "jpg" format from:

http://arXiv.org/ps/astro-ph/0605142v1

This figure "f9.jpg" is available in "jpg" format from:

http://arXiv.org/ps/astro-ph/0605142v1

This figure "f10.jpg" is available in "jpg" format from:

http://arXiv.org/ps/astro-ph/0605142v1

This figure "f11.jpg" is available in "jpg" format from:

http://arXiv.org/ps/astro-ph/0605142v1

This figure "f12.jpg" is available in "jpg" format from:

http://arXiv.org/ps/astro-ph/0605142v1

This figure "f13.jpg" is available in "jpg" format from:

http://arXiv.org/ps/astro-ph/0605142v1

This figure "f14.jpg" is available in "jpg" format from:

http://arXiv.org/ps/astro-ph/0605142v1

This figure "f15.jpg" is available in "jpg" format from:

http://arXiv.org/ps/astro-ph/0605142v1